When all intermetallics dealloy in AA2024-T3
Quantifying early stage intermetallic corrosion kinetics under immersion

Olgiati, Matteo; Denissen, Paul J.; Garcia, Santiago J.

DOI
10.1016/j.corsci.2021.109836

Publication date
2021

Document Version
Final published version

Published in
Corrosion Science

Corrosion Science 192 (2021) 109836

Contents lists available at ScienceDirect

Corrosion Science

journal homepage: www.elsevier.com/locate/corsci

When all intermetallics dealloy in AA2024-T3: Quantifying early stage intermetallic corrosion kinetics under immersion

Matteo Olgiati, Paul J. Denissen, Santiago J. Garcia *

Novel Aerospace Materials group, Aerospace Structures and Materials department, Delft University of Technology, Kluyverweg 1, Delft 2629, HS, The Netherlands

ARTICLE INFO

Keywords:
Local corrosion
Intermetallics
Local electrochemistry
Dealloying
Corrosion mechanisms

ABSTRACT

A hyphenated optical-electrochemical technique and image analysis protocol is used to quantify global and local (intermetallic) corrosion process and kinetics. Our findings reveal an early stage (< 60 s) composition-dependent hierarchical local activation of all IMs that can be attributed to IM dealloying. This is followed by local trenching initiated at matrix locations adjacent to regions of the IMs previously dealloyed, which in turn develops into concentric trenching around the IMs. These stages have quantifiable activation times and kinetics. While dealloying kinetics are found to be strongly dependent on IM composition and slightly dependent on IM size in the case of the S-phases, trenching kinetics are IM composition and size independent.

1. Introduction

The lightweight aluminium alloy AA2024-T3 is a paramount material in the aviation industry due to the good balance between mechanical properties and density [1]. Nevertheless, the heterogeneous distribution of alloying elements (Cu, Mg, Mn and other elements in smaller quantities) across the microstructure, decreases the alloy's intrinsic corrosion resistance and makes it susceptible to local corrosion [2–9]. Microstructural features, such as intermetallic (IM) second phase constituents (> 0.5 μm), were shown to play a major role in the initiation of local corrosion, which has been so far extensively explained through the model of micro-galvanic corrosion, *i.e.* local composition differences between the IM particles and the surrounding Al-rich matrix translate into local differences in Volta potential [10–12], making IMs appear as anodic or cathodic.

Due to the large distribution of IMs compositions, together with the presence of both equilibrium and non-equilibrium IM stoichiometries [2,13], microstructurally-driven corrosion of AA2024-T3 appears in a multitude of diverse forms, morphologies and rates, which are still nowadays difficult to systematise and understand. Historically, presence or abundance of certain elements in the secondary IM phases has been the primary criterion to attribute them an anodic or cathodic character with respect to the Al-rich matrix. This has led to the generally accepted classification for IM particles into two major groups [14]: (i) reactive particles with active elements (*e.g.* Mg) and (ii) noble particles with elements more noble than aluminium (*e.g.* Cu and Fe). In this regard, many studies experimentally showed that Mg-rich particles such as the S-phase (Al_2CuMg) typically undergo anodic dealloying of active elements like Mg and Al, leaving Cu-enriched nanoclusters as remnants [15–19] to become cathodic. On the other hand, particles like AlCuFeMn are regarded as cathodic, thus causing the surrounding Al-rich matrix to be anodically dissolved in a trenching and pitting process due to the local changes in electrolyte's chemistry [18,20–22].

Regardless of the mechanism leading to local IM corrosion, the inevitable result is the formation of corrosion pits due to either dissolution of the particle (dealloying) or cathodic undermining (trenching) with consequent particle detachment (etch out) [23–25]. Further propagation of corrosion pits underneath the surface can in turn lead to intergranular attack of the grain boundaries and the nucleation of corrosion cracks [26–32]. Corrosion pits can therefore act as stress concentrators and reduce the load bearing capacity of the structure in question, eventually resulting in dramatic failures. Due to the serious safety issues in the aerospace field and the high costs associated to corrosive degradation, understanding localised corrosion phenomena in AA2024-T3 and other age-hardened Al alloys has always covered a crucial role in scientific research. A detailed description and understanding of AA2024-T3 corrosion from the very early stages of its initiation is extremely useful for a reliable and damage-tolerant estimation of the overall state-of-corrosion, as well as for a more accurate design and selection of protective systems (*e.g.* conversion coatings, primers, corrosion inhibitors, *etc.*).

Given the relation between microstructure and the onset of local

* Corresponding author.
E-mail address: s.j.garciaespallargas@tudelft.nl (S.J. Garcia).

https://doi.org/10.1016/j.corsci.2021.109836
Received 8 June 2021; Received in revised form 27 August 2021; Accepted 7 September 2021
Available online 10 September 2021

electrochemical degradation, visualisation and characterisation of early-stage corrosion in AA2024-T3 benefits from the use of techniques yielding lateral resolutions in the range of μm or nm, *i.e.* comparable to the dimension of IM second phases and their crystallographic features. For instance, significant efforts have been devoted to study the mechanism of AA2024-T3 local corrosion by means of electron imaging techniques (SEM-EDS [18,33,34], TEM [35–38] and electron tomography [39]), scanning probe microscopies (AFM and SKPFM [9,11,40–43]), X-ray-computed tomography [44] or localised electrochemical tests (LEIS [45], microcapillary test [12,46], SVET [19] or SECM [47,48]). Despite successful and informative, many of these techniques might present some limitations. High-spatial resolution microscopies like SEM and TEM, for example, allow to visualise micro-corrosion features in detail, but their experimental set-ups require high degrees of vacuum, thereby not being always compatible with the corrosive atmospheres/electrolytes to which the alloy is typically exposed. In this way, the use of such techniques has mostly been limited to ex-situ analysis with the consequent loss of temporal resolution and out-of-equilibrium information, as the sample needs to be purposefully removed from the corrosive solution to perform the desired analysis. Recent works, as those of Malladi et al. [49] and Kosari et al. [24,25], have attempted to overcome these limitations by using environmental TEM set-ups to investigate sub-micron corrosion under immersion in *in-situ* or quasi *in-situ* conditions. These studies brought significant novel understanding on the electrochemical properties of individual Cu-rich IM particles exposed to corrosive solutions, although in exchange for a loss of information on the global corrosion behaviour of the alloy and on the potential co-operation between multiple IMs in the formation of stable pits [50], as it commonly happens with highly localised techniques.

In the current work, we introduce the potential use of highly-resolved optical microscopy to study early stage local corrosion processes *in-situ* (*i.e.* under immersion) at quasi real time of immersion. In line with our previous studies [51,52], we used a hyphenated optical-electrochemical set-up combining optical microscopy at high spatial resolution (3 pixels·μm^{-1}) simultaneously with classic electrochemical testing (in this case, electrochemical potential noise measurements). This allows to prevent the loss of information during the early seconds of exposure to the electrolyte and to acquire complete time-dependent information at high optical resolution. With the support of an appropriate post-processing image analysis protocol and a dedicated SEM-EDS inspection of the exposed metal surface prior to immersion, we were able to study and quantify the kinetics of the local corrosion processes related to intermetallics in AA2024-T3 as a function of the immersion time. The optics-based protocol allowed us to visualise the origin of corrosion initiation in relation to the composition of the IM secondary phases. The high temporal and spatial accuracy of the optical measurements performed during immersion unveiled that all identified IMs (independently of their composition) locally behave as anodic in the first seconds to minutes of immersion, yet with composition-dependent kinetic differences.

2. Experimental

2.1. Materials

Commercial grade bare AA2024-T3 was supplied by Kaiser Aluminium in 2 mm thick rolled sheets. The metals were prepared as described in Section 2.2.1.1 and used as working electrode (WE) in the optical-electrochemical set-up. A 0.05 M NaCl aqueous solution (> 98% purity NaCl in "Millipore Elix 3 UV" treated water) was used as corrosive medium.

2.2. Experimental protocols

The experimental protocols followed in this research are schematically shown in the flow chart reported in the Supporting Information 1 (Fig. S1), where a distinction between the methods used before, during and after the immersion of AA2024-T3 in 0.05 M NaCl is made. The following sections will elucidate better on each of these stages.

2.2.1. Analyses before immersion

2.2.1.1. Preparation of AA2024-T3 micro-electrodes. In order to be able to follow local degradation processes (*e.g.* IM attack) with high space-temporal optical resolution, and to relate this information to the electrochemical signals obtained simultaneously, it was necessary to prepare micro-electrodes fitting in the microscope's field-of-view at the maximum spatial resolution possible. Fig. 1a and b show a scheme and a photograph of the prepared AA2024-T3 micro-electrodes used in this study. The steps followed to prepare the microelectrodes are thoroughly described in the Supporting Information 2. During the preparation, a maximal size of 500 × 500 μm^2 was aimed for, but the produced micro-electrodes often resulted in smaller surface areas, which could be, nonetheless, accurately calculated thanks to the SEM analysis described in Section 2.2.1.2.

2.2.1.2. SEM-EDS analysis. Prior to immersion in the corrosive electrolyte, the AA2024-T3 micro-electrodes were analysed with SEM-EDS. Such pre-immersion analysis allowed to identify the composition and spatial location of the IMs present in the surface to be exposed to the electrolyte. For this purpose, an SEM (JEOL JSM-7500F field emission scanning electron microscope coupled with energy dispersive X-ray spectroscopy) was set on back-scattered electrons (BSE) mode. Images were collected with 15 kV of accelerating voltage and 10 μA of emission current. To obtain a higher resolution on the final image, a high magnification (500X) was used and the surface was mapped in six steps (*i.e.* six quadrants). Details of the acquisition procedure are described in the Supporting Information 3.

EDS spectra of the IM particles were obtained *via* point analysis under the same conditions. The IMs were then grouped in four types depending on their detected composition. For an easier identification, a colour code was also established: (i) S-phase (Al_2CuMg, blue), (ii) AlCuFeMn (red), (iii) $(Al,Cu)_x(Fe,Mn)_ySi$ (green) and (iv) not analysed (yellow). The EDS spectra are reported in the Supporting Information 4.

2.2.1.3. Cleaning before immersion. After the SEM-EDS analysis, the micro-electrodes were supposed to be immersed in the corrosive solution. In order to remove possible traces of organic contaminations coming from the SEM-EDS analysis, the micro-electrodes surfaces were quickly re-polished (≈ 10 s) with 1 μm diamond paste, rinsed and sonicated in ethanol for one minute and thoroughly dried in N_2.

2.2.2. Analyses during immersion

Corrosion behaviour of AA2024-T3 immersed in 0.05 M NaCl was evaluated with a hyphenated optical-electrochemical set-up, which allows simultaneous acquisition of electrochemical signals and optical micrographs of the active surface under immersion. In essence, the hardware and software of the set-up used in this work are comparable to the ones in our previous works, where the technique was introduced [52], although the image analysis procedure is different as shown in Section 2.2.3. A detailed description of the set-up including the electrochemical cell and optics is provided in the Supporting Information 5 and its schematic depiction is reported in Fig. 1c. In short, the set-up allows to obtain optical images during immersion at a 1 s resolution together with electrochemical signals information as function of the immersion time (electrochemical potential noise measurements in this work).

Influence of non process-related vibrational and electrical noise were reduced by placing our set-up on an optical table (Nexus, Thorlabs) covered with a large Faraday cage. This allowed for a higher resolution and stability than in previous works. The electrochemical and optical

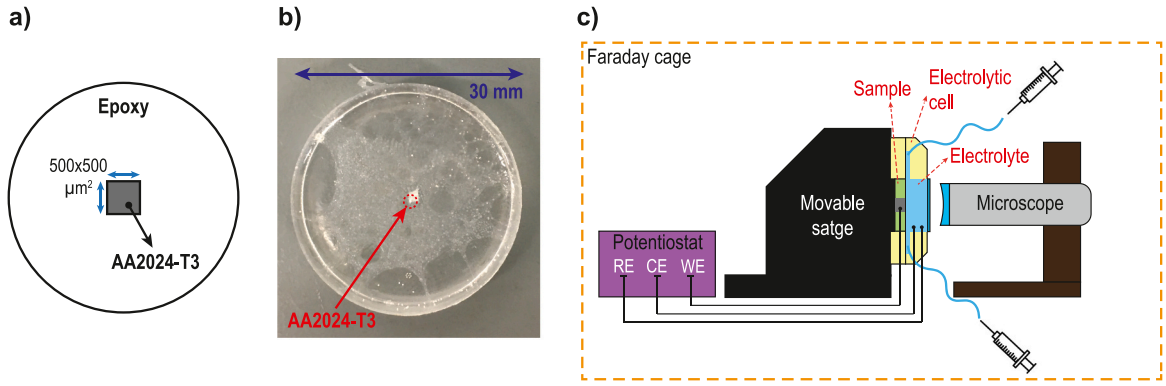

Fig. 1. (a) Schematic top-view and (b) actual image of the prepared AA2024-T3 microelectrodes. The red arrow in b) indicates the location of the micro-electrode (500 × 500 μm^2). The red arrow in (b) indicates the location of the micro-electrode in the epoxy holder. (c) Schematic representation of the opto-electrochemical experimental set-up used in this study. The working distance between the WE surface and the microscope's focal point is ≈ 11.3 mm.

analyses were run in parallel and right after the electrolyte was pushed with a syringe in the electrochemical cell, thereby allowing quasi-immediate monitoring of the corrosion process and a quasi-linear relation between electrochemical signals and optical information. The total immersion time was equal to 1 h (*i.e.* 3600 s) and the final optical resolution was close to 0.3 μm (*i.e.* 3 pixel·μm^{-1}). Tests were repeated in duplicate to validate the method and analysis.

2.2.3. Analyses after immersion

2.2.3.1. Retrieval of IMs spatial coordinates from SEM images. During the immersion experiments, optical images do not allow to fully identify intermetallics, despite the high resolution obtained. To be able to relate local degradation to IM composition and electrochemical signals, it was necessary to design an image analysis protocol capable to locate the IMs identified in the SEM-BSE analysis on the optical images. Adobe Photoshop and ImageJ were the main programmes used for this scope. The details of such protocol are clarified in the Supporting Information 6. In short, this procedure enables to "extract" information about the IMs, acquired through SEM-EDS analysis (such as their shape and spatial position on the micro-electrode surface, as well as their composition), and transpose them with good approximation on both the optical images collected and the resulting activity maps (described in Section 2.2.3.2). This process ultimately allows the relation between the local corrosion processes monitored during immersion, the local IM composition variations and the electrochemical signals collected in parallel to the optical images.

2.2.3.2. Image analysis protocol to quantify surface activity as a function of the immersion time. The image analysis protocol reported previously [52] and based on ImageJ was used to process the optical images obtained during immersion and quantify the evolution of the local surface activity with time. The protocol leads to activity maps where a colour code represents the local degrees of activity. This protocol identifies as "activity" related to corrosion the differences in intensity between pixels at two defined times (time 0 and time t) in a preselected Region of Interest (ROI). In this work, activity maps were created to (i) calculate the global activity map using all the exposed metal surface as the ROI, and (ii) calculate local activity maps for a range of IMs (*i.e.* activity maps at and near IMs) where local ROIs around IMs were selected. The degree of activity is translated into a colour scale whose definition is reported in the Supporting Information 7.

In brief, the protocol consists of the following steps: (i) recursive repositioning of the images to remove misalignments; (ii) evaluation of the pixel-by-pixel time-dependent intensity differences; (iii) increase of the static lower threshold to remove shot noise effects and (iv) calculation of the optically-changed pixels according to the following equation:

$$S_{changed}\ \%\ (t) = \frac{N(t)}{N_{TOT}} \times 100\ \ (\%) \quad (1)$$

where N(t) is the number of changed pixels at generic time t, while N_{TOT} is the total number of pixels in each image or, in other words, the ROI. In this regard, N_{TOT} in the calculation of the global activity maps is ~ 10^6 pixels^2 (*i.e.* pixels belonging to the entire exposed metal surface) while the N_{TOT} used on the local activity maps around each specific IM particle is ~ 10^2-10^3 pixels^2, depending on the specific IM particle size. The selection of N_{TOT} for local activity maps was performed so that the whole IM constituent and no other major constituents (> 0.5 μm) were included in the ROI. In this way, we were able to isolate the activity/kinetics of the individual IM particle without including the (optical) effects of the neighbouring IMs. This selection of N_{TOT} should be considered when attending at the $S_{changed}$ (%) differences between global and local analysis here reported.

The $S_{changed}$ (%) denotes the percentage of the ROI that changes with the immersion time, which, for the solutions and immersion times used in this study, is related to local corrosion processes summed up to give an idea of the corrosion kinetics and extent.

In the present study, we also made the following improvements to this protocol to obtain higher accuracy:

1. Due to the higher resolution achieved with the current experimental set-up, we were able to reduce the static threshold to a lower bin limit of 20 instead of 30. This allowed to accept more optical events in the analysis, thereby avoiding loss of important information. The consequent increase in nuisance (shot noise) in the resulting images is typically characterised by individual or coupled pixels (outliers) uncorrelated with the main optically active regions and was successfully removed by applying a median filtering procedure (neighbours within a radius of 0.5 and threshold = 20).
2. For a better visualisation of optically active areas, we systematically removed background effects by masking the unchanged pixels and transposed the changed (*i.e.* active) ones into a colour scale (reported in the Supporting Information 7) representing the degree of activity.

3. Results and discussion

3.1. Relation between OCP time evolution and optical changes

Fig. 2 shows the time evolution of the electrochemical potential (OCP, black curve) and the global electrode activity quantified from the optical images ($S_{changed}$ %, red curve) during the first hour of immersion in 0.05 M NaCl. The calculated IM surface coverage (1.47%, green dashed line) is included for reference. In the OCP evolution with time,

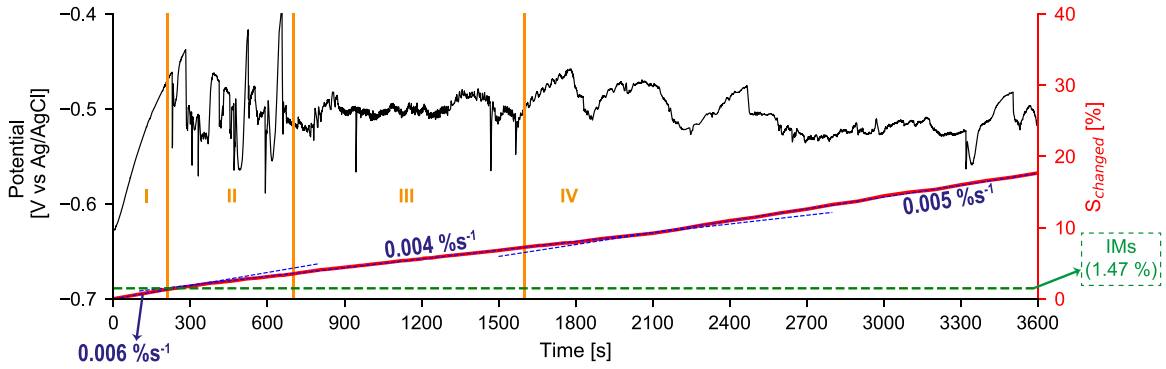

Fig. 2. Time evolution of the electrochemical potential (OCP, black line) and the active surface area measured by *in-situ* optics ($S_{changed}$ %, red curve) for AA2024-T3 immersed in 0.05 M NaCl for 3600 s. For reference the surface area originally covered by intermetallics is included as a green dashed line.

four different regimes (labelled as I, II, II and IV) can be clearly recognised:

- Stage I: From 0–200 s there is a steep, but "noise"-free OCP increase (approx. 150 mV) towards more noble OCP values;
- Stage II: From 200–700 s the OCP becomes unstable with presence of frequent high amplitude (150 mV) fluctuations normally referred to as transients;
- Stage III: From 700–1600 s the OCP curve is still characterised by frequent transients (unstable oscillations), though with remarkably reduced amplitude (min 10 mV, max 60 mV);
- Stage IV: From 1600–3600 s long duration OCP variations are observed together with some transients of low amplitude.

Despite the electrodes used in this study are significantly smaller than those used in previous works [52–54], the four identified regions and overall OCP trend are similar to those previously reported, thereby

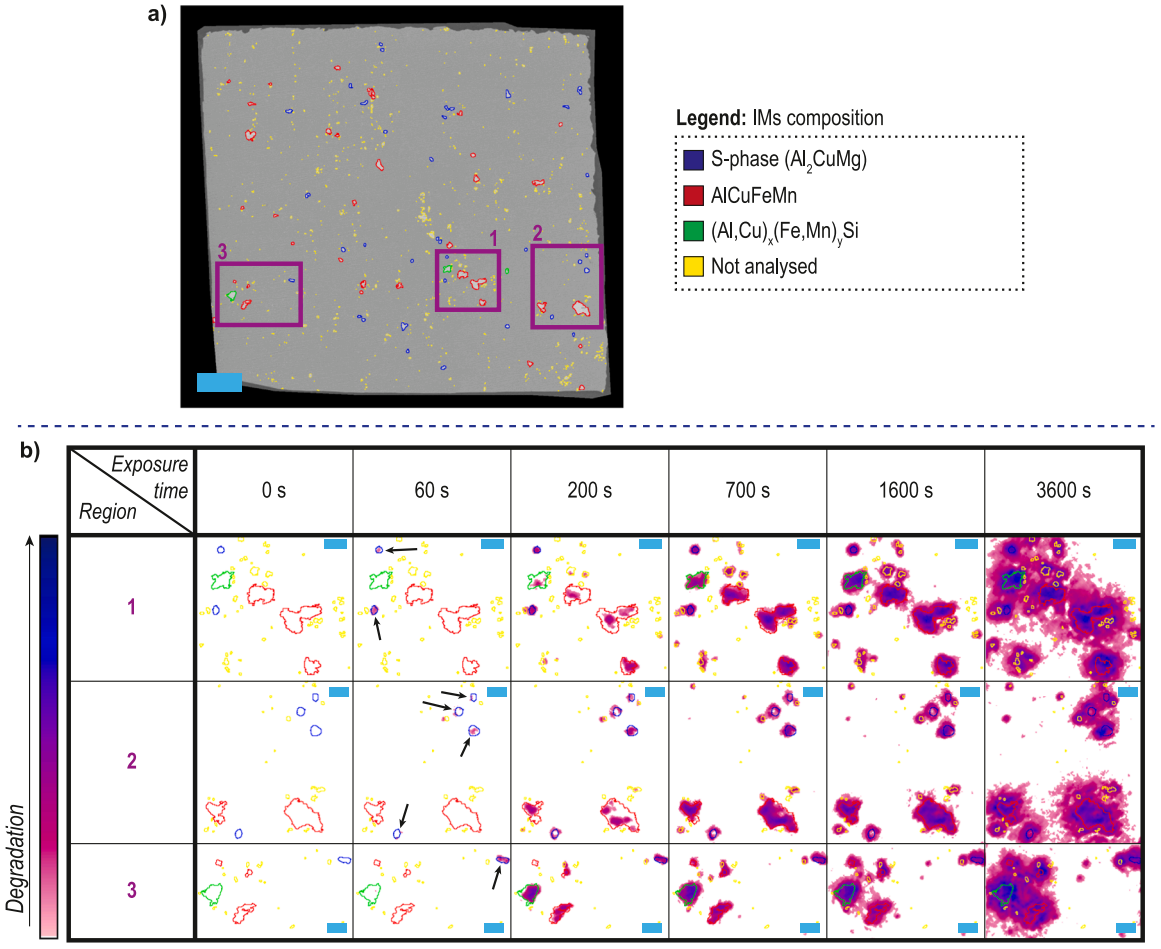

Fig. 3. (a) Reconstructed SEM-BSE image of the micro-electrode surface with IM particles of diverse composition highlighted in different colours (Al_2CuMg – blue; AlCuFeMn – red; $(Al,Cu)_x(Fe,Mn)_ySi$ – green; not identified – yellow). The blue scale bar represents 50 μm. (b) Time evolution (at 0, 60, 200, 700, 1600 and 3600 s) of the optical activity at three representative selected areas, marked in (a) as 1, 2 and 3, containing IMs of both known (blue, red and green) and unknown (yellow) compositions. These images are cropped from the activity maps generated in the global activity analysis. The scale bars in the local activity maps represent 10 μm.

confirming the validity of small micro-electrodes for such studies. The optical results ($S_{changed}$) show three stages of slightly different degradation kinetics (represented by the blue slopes in Fig. 2), which are in overall good agreement with those reported in our previous work using larger electrodes [52]. The first kinetic stage (0.006%s^{-1}) coincides with the Stage I in the OCP trend and the first ≈ 300 s of immersion. The second kinetic stage is a bit slower (0.004%s^{-1}) and extends across the Stages II and III of the OCP trend. In the final stage, the surface degradation process accelerates again (0.005%s^{-1}) and roughly coincides with the Stage IV of the OCP trend. As observed in our previous work [52], at around 200 s of immersion, the total affected surface area coincides with the total area covered by intermetallics (≈ 1.5%). In a first order approximation, this could indicate that all the corrosion activity is localised at the IMs during the first 200 s and extends beyond the IM area after 200 s immersion. It should be noted that this result suggests that local activity (*e.g.* dealloying) at IMs happens significantly faster than previously reported based on *ex-situ* optical analysis [18] or lower resolution optics during immersion [51] (⩾ 5 min) using comparable salt solutions and alloy. Nevertheless, to gain a better understanding on the relation between IM composition and local activity a more detailed analysis is necessary, as discussed in Section 3.2.

3.2. Local degradation as function of IM composition

To identify differences in local degradation kinetics as function of the IM constituent composition, an EDS analysis of the IMs was performed prior to immersion. Fig. 3a shows a SEM-BSE image of the microelectrode surface, where the brighter IM particles, richer in elements with high atomic number (*e.g.* Cu), can be easily discerned from the darker Al-rich matrix. The elemental composition analysis allowed grouping the IMs according to their major alloying elements, which was visualised by assigning a different colour to each IM composition

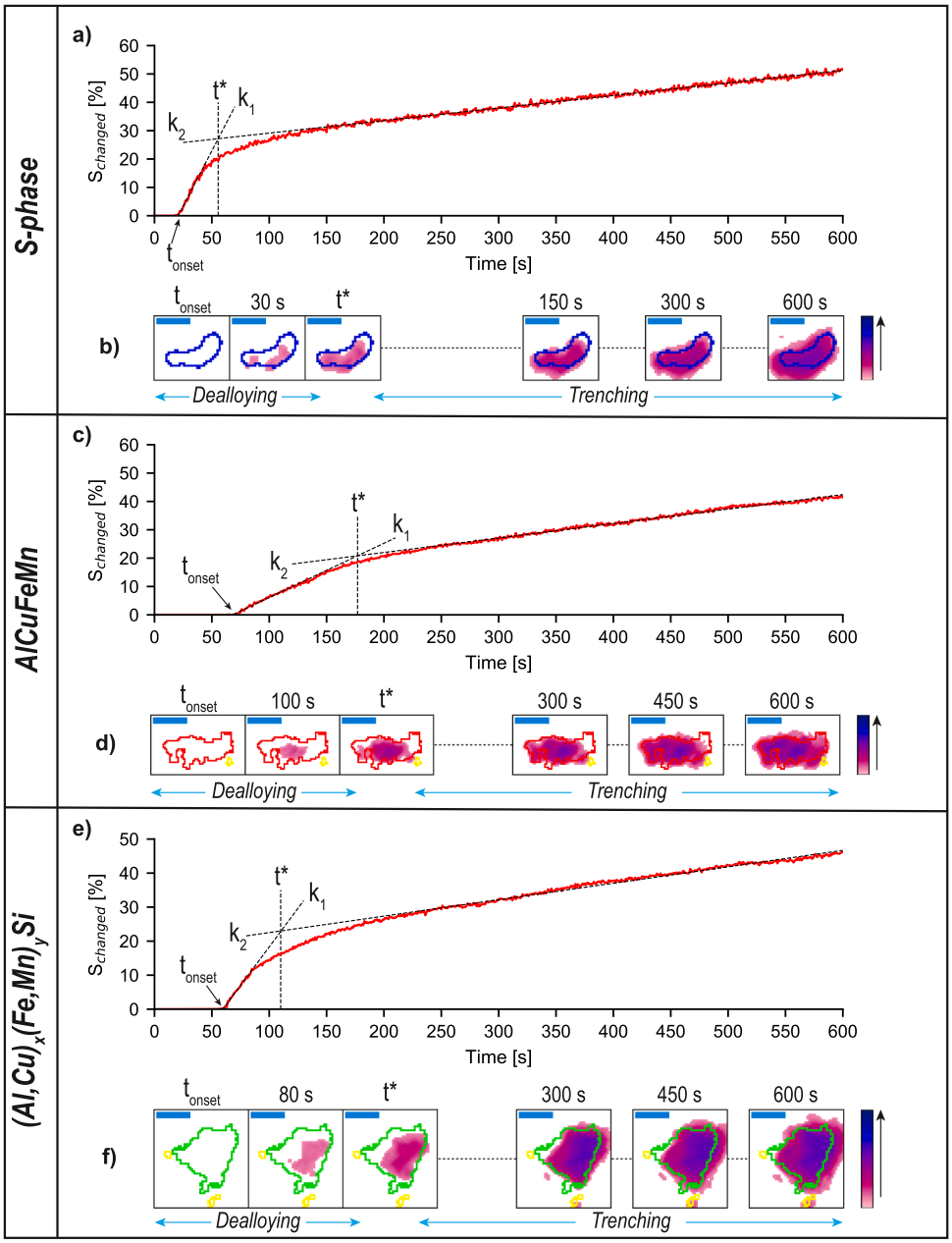

Fig. 4. (b), (d) and (f) Individual IM activity maps and (a), (c) and (e) their calculated degradation kinetics (Schanged (%) during the first 600 s of immersion. (a) and (b), (c) and (d), (e) and (f) correspond to representative IM particles S-phase, AlCuFeMn, and $(Al,Cu)_x(Fe,Mn)_ySi$, respectively. k_1, k_2, t* and t_{onset} are the representative kinetic parameters of the intermetallic degradation process. The blue scale bars at the top left corner in each local activity map represent 5 μm.

(Fig. 3a). It is important to note that, for the scope of this study, we were not interested in determining the exact stoichiometry of each constituent in detail, but rather have a qualitative idea of the phases' distribution across the surface. For this reason, we classified the IMs based on the relative abundance of certain elements following the indications in [18]: particles rich in Cu and Mg were coloured blue and classified as S-phases (Al_2CuMg), particles containing Cu, Fe and Mn were denoted as generic "AlCuFeMn" phases and coloured red, while particles containing Cu, Fe, Mn and Si were denoted as $(Al,Cu)_x(Fe,Mn)_ySi$ and coloured green. Furthermore, we only determined the composition of a few IMs among the biggest constituents (> 1 μm), since local macroscopic events taking place on these are more likely to be resolved by our optical camera during the test. Despite visible in the SEM-BSE map, the smaller particles (*e.g.* dipersoids, 50–500 nm), whose size is comparable or smaller than the EDS spatial resolution limit (*i.e.* spot size of a few μm), could not be accurately analysed in their composition. For this reason, all the non-analysed constituents and dispersoids were highlighted as yellow, in order to acknowledge their presence (and thus monitor possible localized phenomena) during the analysis.

As a result of the procedure described in Section 2.2.3.1, the coordinates, shapes and colours (*i.e.* compositions) of the IMs could be easily traced back in the optical images collected during immersion, thereby being able to relate local activity to IM composition. For clarity we show only three representative areas (labelled as 1, 2 and 3 in Fig. 4a), containing IM phases of all compositions. Fig. 3b shows three areas representative of the overall sample degradation cropped from the images obtained during the global activity map analysis (Fig. 3a) as a function of the immersion time. The selected immersion times (0, 60, 200, 700, 1600 and 3600 s) are chosen in agreement with the identified OCP regions reported in Fig. 2. The colour bar represents the degree of optical activity and, consequently, degradation. The global activity map (for the entire working electrode surface) overlapped with the IM contours can be found in the Supporting Information 10.

From the activity maps in Fig. 3b the following observations can be derived in relation to the four regions identified in the OCP signal analysis:

- **Stage I (0–200 s):** In the first 60 s of immersion clear localized attack happens at S-phase IMs (indicated in the selected areas with arrows at 60 s). Between 60 and 200 s of immersion, activity extends to all other IM compositions as can be seen with the appearance of purple colour at the green- and red-marked IMs at 200 s in Fig. 3b, as well as in some yellow IMs. This activity, localised exactly at the IMs surface, coincides in time with the Stage I observed in Fig. 2 showing a steep potential increase towards more positive potentials and may, therefore, be attributed to a hierarchical activation of localised corrosion at IMs, as suggested elsewhere [18].

  The early-stage attack of S-phases has been widely reported in other studies, yet at significantly longer immersion times, and is believed to be ascribed to the (anodic) dealloying of less noble elements, such as Mg and Al [55]. The other IM phases (red and green), on the other hand, are commonly believed to behave as cathodic particles based on reported OCPs [2,11,12], thus supporting oxygen reduction reactions (ORR), changing the local chemistry of the electrolyte, favouring the alkaline dissolution of the aluminium oxide layer on the surrounding Al-rich matrix and, eventually, promoting the nucleation of corrosion pits ("trenches") around the particle [56]. However, the behaviour observed for these particles with our opto-electrochemical set-up seems to deviate remarkably from this model, at least during the first minutes of immersion: First, the potential and optics give evidence of discrete local corrosion events (transients, "trenching") only after 200 s. Secondly, the corrosion attack nucleates inside the particles themselves rather than being limited to the peripheral interphase region as can be seen at 200 s for a couple of red and green particles, where the purple colour indicating activity is localized within the IM. In other words, the optical and electrochemical data indicates that all IMs are locally active during the very first minutes of immersion in the absence of galvanic couple induced trenching. Two phenomena can potentially explain the observed local activity at IMs: (i) dissolution of the native oxide layer on top of the IM particles under the action of Cl^- ions [43,57] or/and (ii) local IMs dealloying. As for the first option, it seems that the optical microscope is not sensitive enough to detect thickness variations at such low scale (nm). The second option (local IM dealloying) seems more plausible at this stage. Previous studies, for instance, reported that IM particles can sometimes manifest with complex microstructures entailing multiple phase domains [36,58–61]. Such local compositional differences could lead to (nano) galvanic couplings between a less and a more noble domain within the same IM, thus determining the preferential dissolution of one domain (more anodic) at the expenses of the other (more cathodic). In this regard, Zhang et al. stated in their work [37] that IM-specific galvanic interactions may not be necessarily related to the presence of compositional domains, but they can also stem from inherent crystallographic inhomogeneities of the IM microstructure. In particular, they were able to demonstrate with the use of HAADF-STEM that initial dealloying of Al and Mn from $Al_{20}Cu_2Mn_3$ particles (T-phase) is the result of an atomic-scale galvanic interaction between T-phase and twin boundaries where preferential Cu segregation takes place. Similarly, Kosari et al. also used quasi *in-situ* STEM/EDS to report the early formation of nano-pits and dealloyed regions over isolated constituents like $Al_{76}Cu_6Fe_7Mn_5Si_6$ and $Al_7Cu_2Fe(Mn)$ [25]. The same authors also reported a dealloying-driven self-corrosion mechanism for the presumably cathodic θ-phases (Al_2Cu) observed with *in-situ* HAADF-STEM [24], as previously observed by Zhang et al. [62].

  Although our optical instrumentation is inherently not capable of achieving the same spatial resolutions of TEM microscopes used in other studies, we cannot exclude that the obvious activity detected with our optical analysis at the IMs during the first 200 s of immersion could be a direct consequence of the previously hypothesized dealloying-driven events, resulting from the microstructurally-intrinsic and numerous nano- or atomic-scale galvanic cells spread across the secondary particles' surfaces. On balance, we can assume that the first 200 s of immersion could be dominated by initial dealloying and (selective) self-dissolution events of all the IM constituents. This suggests that, besides the well-reported case of the S-phase, all IMs studied behave locally anodic during the very first seconds-to-minutes of immersion. This is in contradiction to the reported cathodic OCPs of some of them (*e.g.* AlCuFeMn and $(Al,Cu)_x(Fe,Mn)_ySi$), which might be attributed to their individual potentials being traditionally measured already after dealloying, due to the almost unavoidable waiting time between exposure to electrolyte and measurement. This hypothesis of overall anodic activity at IMs during early stage of immersion is supported by the ennoblement observed in the electrochemical potential trend in this period, presumably due to the dissolution of less noble elements from the IMs and subsequent enrichment in more cathodic elements.
- **Stage II (200–700 s):** The appearance of fast high-amplitude fluctuations in the OCP signal, corresponds to the consolidation of the activity inside the IM constituents, which also show higher intensity, but also to the propagation of the activity beyond the IM boundaries into the surrounding interfacial Al-rich matrix. Previous studies on ferrous alloys already suggested the existence of a relation between noise transients and the nucleation of corrosion pits [63,64], which, in the case of AA2024-T3, could be associated to metastable and stable "trenching" around IMs [52,65]. The results also agree with the previously reported observation of trenching around presumably cathodic phases like AlCuFeMn and $(Al,Cu)_x(Fe,Mn)_ySi$, but also around dealloyed S-phase residuals [17,21]. It was previously reported that dealloying of the most active elements in S-phases (Mg

and Al) generates porous Cu-enriched remnants [24], as well as detached CuO_2 globular nanoclusters after complete dealloying (though at longer immersion times) [19,24,38,66], thereby locally increasing the nobility and cathodic activity of S-phases and, consequently, accelerating the dissolution of the adjacent Al-matrix. The results suggest that a similar dealloying model, albeit at lower time scale, could be an indication that trenching phenomena around the IMs, as well as the consequent formation of corrosion products (such as $Al(OH)_3$ gel) directly around the pits, become active and dominant at this stage. Although some minor area fractions of the interfacial Al-rich matrix become optically affected in this stage, the global activity is still highly localised on the IM phases and their vicinity.

- **Stage III (700–1600 s):** In this exposure period, the OCP trend shows a reduction of the transients' amplitude and a stabilisation of the signal, which suggests a stable propagation of corrosion proceeding at an almost constant OCP value (≈ -0.5 V *vs* Ag/AgCl in Fig. 2), most likely the corrosion potential (E_{corr}) of the alloy at thermodynamic equilibrium. Isolated transients of greater amplitude ($\approx$ 50 mV), perhaps indicating the nucleation of new pitting events, are still visible in the signal, despite becoming more and more limited in number. The results observed in the local activity maps, on the other hand, indicate further radial growth of corrosion from the previously activated IMs: the optically active areas are now exceeding the boundaries of IM particles more remarkably, although the IMs substantially remain the primary centres of activity. This leads us to the assumption that stable growth of the pits, nucleated around the IMs during previous stages of immersion, becomes favoured towards the bulk of the electrode ("subsurface"). Since subsurface corrosion is less accessible to the microscope, the optical analysis does not provide direct evidence of such events. Nevertheless, the substantial lack of new significant initiation events (*e.g.* the majority of the Al-rich matrix beyond the IMs remains unaffected) together with the high degree of activity being localised on and around the IM phases, indirectly points at electrochemical activity mainly occurring underneath the surface within a pitting morphology. Some studies also pointed out that subsurface growth of trenches may lead to IM undercutting and, eventually, particle detachment [24,25], but this seems undetected optically or electrochemically (OCP) as individual events in this work.
- **Stage IV (1600–3600 s):** The OCP signal in this stage shows a significant reduction in transients and frequency with an overall an unstable character. The global activity maps in Fig. 3b show continuous propagation of local activity beyond the IMs and propagating over the Al-rich matrix. The shape of the newly activated areas is quite irregular in this stage, *i.e.* non-concentric growth as happened in previous stages yet still associated to the active IM centres. For long immersion times, other studies described the corrosion process to be taking place mainly underneath the surface with pit propagation to the grain boundaries and consequent intergranular attack [26,50]. As such subsurface processes are not directly observable, the optical activity detected in this stage is more likely to be associated to further deposition and thickening of (hydr-) oxides as corrosion products, stemming from localized trenching and pitting processes.

3.3. Intermetallic degradation kinetics as function of composition

The results shown in Fig. 3b seem to suggest that degradation initiates inside the IM particles at first, regardless of their composition, probably due to self-dealloying events (*i.e.* locally anodic). After this, it propagates beyond the IM boundaries in the form of trenches. Despite we suggest all IMs follow a similar self-degradation phenomenology, important differences in relation to their kinetics of degradation as function of the IM composition are likely to exist and are largely underreported. The protocol here introduced allows us to study the local degradation kinetics of individual IM constituents more in depth by restricting the activity quantification analysis to a number of individual particles of different composition. To this purpose, we selected 5 blue particles (S-phases), 5 red particles (AlCuFeMn) and 3 green particles ($(Al,Cu)_x(Fe,Mn)_ySi$), as these last ones were less abundant than the rest, and repeated the image analysis for each one of them to obtain individual particle activity maps and kinetic information. Fig. 4 shows, for three representative particles, the local activity maps (Figs. 4b, d and f) and their calculated degradation kinetics $S_{changed}$ % (Fig. 4a, c and e) during the first 600 s of immersion, which correspond to the dealloying and trenching initiation stages reported in 3.2.

From Fig. 4a, c and e, a number of observations can be made:

- Activity at IMs is only visible after a time of quiescence, which in all cases was named as t_{onset}. As already seen in Fig. 3b, t_{onset} is lowest for the S-phase IMs.
- After initiation time, the activity observed at and around of individual particles is characterised by two stages, proceeding with different linear kinetics. The first regime is typically faster (greater slope, k_1) than the second (smaller slope, k_2).
- The transition from a faster (k_1) to a slower (k_2) degradation kinetics process is represented by a transition time (t*), identified by the interception point between the two fitting slopes.

The similar shape of the $S_{changed}$ %curves shown in Fig. 4a, c and e was found to be reproducible for the 13 analysed particles (not shown). This could indicate a similar phenomenology of degradation taking place at all the constituent particles, regardless of their composition. Better understanding of the nature of these processes can be gained through the analysis of the corresponding individual IM activity maps reported in Figs. 4b, d and f. In these, we show the surface activity taking place before and after t*. Before t*, surface activity is always observed mainly inside the boundaries of individual IMs (see 30 s in Fig. 4b, 100 s in Fig. 4d and 80 s in Fig. 4f). At t*, the majority of the activity is still localised inside each IM particle, but small portions of the surrounding Al-rich matrix (*i.e.* outside the particle) start to be affected, even though the particle itself has not yet completely undergone degradation (*i.e.* activity). It should be noted that activity outside the particle always initiates in the direct vicinity of previously-degraded areas inside the particles. After t*, activity keeps propagating both inside and outside the particles of different chemistries in a similar manner: when the particle is fully active the activity outside the particle becomes more significant.

These observations further suggest that activity at IMs is most likely related to local self-dissolution events (*e.g.* dealloying) during the earliest stages of immersion, because activity is always observed in the area limited by the particles' boundaries. Such dealloying is comparatively a fast process taking place at a rate equal to k_1 whose magnitude depends on the IM composition. A similarly linear dealloying propagation front has also been reported for Ag-Au single phase alloys [67]. Dealloying in IMs, however, is not uniformly spread across the particle's surface, but might rather take place in a localised way as a consequence of local nanogalvanic cells, as suggested elsewhere [37]. Site-specific dealloying induces a local increase of the cathodic character of the particle, which promotes trenching of the Al-rich matrix in close contact with the dealloyed area. This situation is clearly observed at t*, where degradation outside the particle (most likely associated to nucleation of "trenches") appears only in the vicinity of previously-dealloyed regions within the IM. In other words, t* is a representative transition time of a region (*i.e.* when the curve deviates from the slopes k_1 and k_2) where there is coexistence of events taking place inside (dealloying) and outside (trenching) individual constituents. At longer immersion times ($> t^*$), a larger portion of the IM particles' surface has undergone substantial dealloying and the propagation of trenching on the Al-rich matrix combined with (hydr-)oxides deposition becomes dominant and characterised by a rate equal to k_2, remarkably slower than k_1. The linear increase of the corroded area around IMs due to trenching

phenomena confirms previous reports using different electrolytes and environmental pH conditions [21].

Fig. 5 (as well as Table S1 reported in the Supporting Information 11) shows the characteristic kinetic parameters obtained from the individual IM degradation study as shown in Fig. 4. First, it can be observed that the activity at the S-phases starts significantly earlier ($10\ s < t_{onset} < 30\ s$) than for other phases ($t_{onset} \geqslant 60$ s). This confirms (quantitatively) the hierarchical activation of S-phases observed in Fig. 3b and suggested elsewhere [18]. After t_{onset}, the selective dissolution or dealloying kinetics described by k_1 is almost two times faster for the S-phases than for the other IMs (*i.e.* $\approx 0.5 \pm 0.25\%s^{-1}$ *vs* $\approx 0.2 \pm 0.15\%s^{-1}$, respectively), indicating a higher dealloying driving force. Such a difference may be attributed to the electrochemical activity of the single elements being dissolved from the IM and the strength of the local galvanic couples depending on IM composition. According to literature, S-phases will preferentially dissolve Mg, which is the most active element of the galvanic series, and partly Al. Other phases, on the other hand, are more likely to dissolve Al, Fe or Mn, which typically cover more noble positions in the galvanic series. As a result, S-phases will show earlier and faster selective dealloying due to a stronger internal driving force.

It is suggested that anodic dealloying remains the dominant process on the IMs until the Cu-enriched dealloyed areas start to induce local changes in the electrolyte chemistry due to cathodic OH^- production and consequent pH increase. Other studies have also reported that, in such pH conditions, the Al_2O_3 passive film covering the near Al-rich matrix is destabilised (local breakdown) and trench initiation becomes favoured [21,25]. It is important to note that trench initiation (detected here as activity outside the IMs) was observed near dealloyed regions of the IMs and not elsewhere. This might imply a mutual influence between the two processes of dealloying and matrix dissolution (trenching), as proposed in other works [25]. A transition between a dealloying-dominated stage and a trenching-dominated one is represented by a characteristic t*, which is again composition-dependent. S-phases typically reach t* after only 68 s under immersion, while the other IMs take 3 times more to reach the transition stage. This highlights the intensity of the dealloying process in the S-phases compared to the other IMs. After t*, all IM locations show a radially-growing activity beyond the IM boundaries attributed to trench nucleation and growth. This process, characterized by k_2 is, in all IM cases, significantly slower than the dealloying stage (k_2 is one order of magnitude lower than k_1). Moreover, this second stage proceeds at a comparable rate in all cases which shows to be less dependent on the IM compositional class considered. This result is compatible with the mechanism of trenching being sheer dissolution of the Al-rich matrix around dealloyed IM constituents, which, therefore, leads to relatively similar galvanic couples (*i.e.*, despite compositional differences, the galvanic couples may be similar once dealloyed).

Besides IM composition, the possible effect of IM size and aspect ratio on the temporal (t_{onset} and t*) and kinetic (k_1 and k_2) parameters was further analysed since these could affect the magnitude of the galvanic couple and, thereby, its degradation rate. The results are reported in the Supporting Information 12 (Fig. S11). No clear dependency of t_{onset} and t* with IM size or IM aspect ratio was found for any of the particle compositions, even when S-phases are normally smaller than AlCuFeMn and $(Al,Cu)_x(Fe,Mn)_ySi$,. The hierarchical effect of composition on t_{onset} and t* is therefore more dominant than the geometrical one (*i.e.* t_{onset} and t* are always lower for S-phases compared to AlCuFeMn and $(Al,Cu)_x(Fe,Mn)_ySi$).

As for the early-stage S-phase dealloying, it seems like the degradation rate (k_1) has an apparent relation with both IM size and aspect ratio, which makes it hard to say which of the two dominates. The same relation between k_1 and IM size/aspect ratio is not visible for AlCuFeMn and $(Al,Cu)_x(Fe,Mn)_ySi$. Finally, the trenching-dominated degradation kinetics (k_2) was found to be independent of IM size, aspect ratio or compositional class.

These results suggest that the geometry of IMs might only play a minor role in the IM degradation process compared to the compositional differences. The result is in good agreement with the findings of this work that suggest that IM degradation kinetics (local dealloying) might be triggered by (nano)galvanic couples within the IM constituents (anodic and cathodic regions inside the IM particle) in a similar way dealloying happens in single phase alloys. In this degradation model, lower dependence on IM size than on IM composition is expected as opposite to a local degradation model based on macroscopic electrochemical potential differences between IMs and Al-rich matrix where the anode-cathode ratio should have a greater effect on the degradation kinetics.

4. Conclusions

A hyphenated optical and electrochemical set-up and dedicated image analysis software allowed to study local intermetallic degradation under immersion with high space-temporal resolution. It was found that IM particles of all compositions show anodic local activity during early-stage immersion (under 200 s immersion). Although the activation time of the IM degradation and the degradation kinetics is composition dependent, all IMs showed a similar degradation phenomenology, consisting of: (i) activation time, (ii) rapid early-stage self-dissolution (dealloying) denoted by activity predominantly inside the particle, and (iii) one order of magnitude slower process dominated by "trenching" combined with oxide deposition and denoted by activity both inside and outside each particle. Although the overall behaviour of dealloying and trenching had been proposed for S-phase, this study suggests that a similar process may occur also at IMs commonly believed to behave "cathodic", thus suggesting a possible initial (local) anodic character in most IMs due to local compositional variations.

The intermetallic local activity analysis based on optics developed in

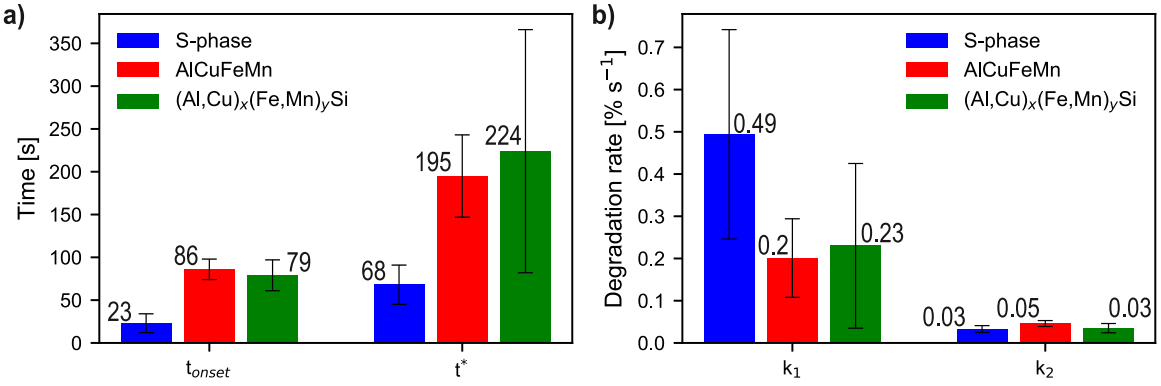

Fig. 5. Quantification of (a) temporal (t_{onset} and t*) and (b) kinetic (k_1 and k_2) parameters, calculated on individual IM particles belonging to different compositional classes (S-phase, AlCuFeMn and $(Al,Cu)_x(Mn,Fe)_ySi$) and expressed as average (coloured bars) with the relative standard deviation (black bars).

this study also suggests that, for the studied conditions, dealloying of S-phases occurs twice as fast as dealloying of AlCuFeMn/$(Al,Cu)_x(Fe,Mn)_ySi$, whereas the second degradation stage, associated to "trenching" and oxides deposition, takes place at similar rates independently of the IM composition and perhaps related to a concentration-driven process like O_2 diffusion. The onset of the IM activity was also found to vary hierarchically between ≈ 25 s for S-phases and ≈ 70 s for AlCuFeMn/$(Al,Cu)_x(Fe,Mn)_ySi$ probably due to composition-dependent driving forces. On the other hand, geometrical factors, such as IMs size and aspect ratio, were found to have a limited impact on the degradation kinetics. IM composition is the main driving force for the local IM dealloying process.

The results here presented provide new insights in the corrosion mechanism of AA2024-T3 with a possible impact on the development of efficient protection strategies (*i.e.* inhibitors).

CRediT authorship contribution statement

Matteo Olgiati: Investigation, Formal analysis, Writing – original draft, Visualization. **Paul J. Denissen**: Methodology, Formal analysis, Writing – review & editing. **Santiago J. Garcia:** Conceptualization, Methodology, Writing – review & editing, Visualization, Supervision.

Declaration of Competing Interest

The authors declare that they have no known competing financial interests or personal relationships that could have appeared to influence the work reported in this paper.

Acknowledgements

The authors thank the Faculty of Aerospace Engineering at the Delft University of Technology for financial support.

Appendix A. Supporting information

Supplementary data associated with this article can be found in the online version at doi:10.1016/j.corsci.2021.109836.

References

[1] A.P. Mouritz, Aluminium alloys for aircraft structures, in: Introd. to Aerosp. Materials, Elsevier, 2012, pp. 173–201, https://doi.org/10.1533/9780857095152.173.
[2] A.E. Hughes, N. Birbilis, J.M.C. Mol, S.J. Garcia, X. Zhou, G.E. Thompson, High strength Al-alloys: microstructure, corrosion and principles of protection, in: Recent Trends Process. Degrad. Alum. Alloy., InTech, 2011, https://doi.org/10.5772/18766.
[3] A.E. Hughes, R. Parvizi, M. Forsyth, Microstructure and corrosion of AA2024, Corros. Rev. 33 (2015) 1–30, https://doi.org/10.1515/corrrev-2014-0039.
[4] C. Blanc, B. Lavelle, G. Mankowski, The role of precipitates enriched with copper on the susceptibility to pitting corrosion of the 2024 aluminium alloy, Corros. Sci. 39 (1997) 495–510, https://doi.org/10.1016/s0010-938x(97)86099-4.
[5] V. Guillaumin, G. Mankowski, Localized corrosion of 2024 T351 aluminium alloy in chloride media, Corros. Sci. 41 (1998) 421–438, https://doi.org/10.1016/s0010-938x(98)00116-4.
[6] P. Leblanc, G.S. Frankel, A study of corrosion and pitting initiation of AA2024-T3 using atomic force microscopy, J. Electrochem. Soc. 149 (2002) B239, https://doi.org/10.1149/1.1471546.
[7] W. Zhang, G.S. Frankel, Localized corrosion growth kinetics in AA2024 alloys, J. Electrochem. Soc. 149 (2002) B510, https://doi.org/10.1149/1.1513984.
[8] C. Blanc, S. Gastaud, G. Mankowski, Mechanistic studies of the corrosion of 2024 aluminum alloy in nitrate solutions, J. Electrochem. Soc. 150 (2003) B396, https://doi.org/10.1149/1.1590327.
[9] K.A. Yasakau, M.L. Zheludkevich, S.V. Lamaka, M.G.S. Ferreira, Mechanism of corrosion inhibition of AA2024 by rare-earth compounds, J. Phys. Chem. B. 110 (2006) 5515–5528, https://doi.org/10.1021/jp0560664.
[10] R.G. Buchheit, A compilation of corrosion potentials reported for intermetallic phases in aluminum alloys, J. Electrochem. Soc. 142 (1995) 3994–3996, https://doi.org/10.1149/1.2048447.
[11] P. Schmutz, G.S. Frankel, Characterization of AA2024-T3 by scanning kelvin probe force microscopy, J. Electrochem. Soc. 145 (1998) 2285–2295, https://doi.org/10.1149/1.1838633.
[12] N. Birbilis, R.G. Buchheit, Electrochemical characteristics of intermetallic phases in aluminum alloys, J. Electrochem. Soc. 152 (2005) B140, https://doi.org/10.1149/1.1869984.
[13] A.E. Hughes, A.M. Glenn, N. Wilson, A. Moffatt, A.J. Morton, R.G. Buchheit, A consistent description of intermetallic particle composition: an analysis of ten batches of AA2024-T3, Surf. Interface Anal. 45 (2013) 1558–1563, https://doi.org/10.1002/sia.5207.
[14] J. Li, J. Dang, A summary of corrosion properties of Al-rich solid solution and secondary phase particles in Al alloys, Metals 7 (2017) 84, https://doi.org/10.3390/met7030084.
[15] R.G. Buchheit, R.P. Grant, P.F. Hlava, B. Mckenzie, G.L. Zender, Local dissolution phenomena associated with S phase (Al2CuMg) particles in aluminum alloy 2024-T3, J. Electrochem. Soc. 144 (1997) 2621–2628, https://doi.org/10.1149/1.1837874.
[16] M.B. Vukmirovic, N. Dimitrov, K. Sieradzki, Dealloying and Corrosion of Al Alloy 2024-T3, J. Electrochem. Soc. 149 (2002) B428, https://doi.org/10.1149/1.1498258.
[17] G.O. Ilevbare, O. Schneider, R.G. Kelly, J.R. Scully, In situ confocal laser scanning microscopy of AA 2024-T3 corrosion metrology: I. Localized corrosion of particles, J. Electrochem. Soc. 151 (2004) B453, https://doi.org/10.1149/1.1764780.
[18] A. Boag, A.E. Hughes, A.M. Glenn, T.H. Muster, D. McCulloch, Corrosion of AA2024-T3 Part I: Localised corrosion of isolated IM particles, Corros. Sci. 53 (2011) 17–26, https://doi.org/10.1016/j.corsci.2010.09.009.
[19] H. Shi, Z. Tian, T. Hu, F. Liu, E.-H. Han, M. Taryba, S.V. Lamaka, Simulating corrosion of Al2CuMg phase by measuring ionic currents, chloride concentration and pH, Corros. Sci. 88 (2014) 178–186, https://doi.org/10.1016/j.corsci.2014.07.021.
[20] T. Suter, R.C. Alkire, Microelectrochemical studies of pit initiation at single inclusions in Al 2024-T3, J. Electrochem. Soc. 148 (2001) B36, https://doi.org/10.1149/1.1344530.
[21] O. Schneider, G.O. Ilevbare, J.R. Scully, R.G. Kelly, In situ confocal laser scanning microscopy of AA 2024-T3 corrosion metrology: II. Trench formation around particles, J. Electrochem. Soc. 151 (2004) B465, https://doi.org/10.1149/1.1764781.
[22] L.B. Coelho, M. Taryba, M. Alves, M.F. Montemor, M.-G. Olivier, Unveiling the effect of the electrodes area on the corrosion mechanism of a graphite - AA2024-T3 galvanic couple by localised electrochemistry, Electrochim. Acta 277 (2018) 9–19, https://doi.org/10.1016/j.electacta.2018.04.187.
[23] Y. Zhu, K. Sun, G.S. Frankel, Intermetallic phases in aluminum alloys and their roles in localized corrosion, J. Electrochem. Soc. 165 (2018) C807–C820, https://doi.org/10.1149/2.0931811jes.
[24] A. Kosari, H. Zandbergen, F. Tichelaar, P. Visser, P. Taheri, H. Terryn, J.M.C. Mol, In-situ nanoscopic observations of dealloying-driven local corrosion from surface initiation to in-depth propagation, Corros. Sci. 177 (2020), 108912, https://doi.org/10.1016/j.corsci.2020.108912.
[25] A. Kosari, F. Tichelaar, P. Visser, H. Zandbergen, H. Terryn, J.M.C. Mol, Dealloying-driven local corrosion by intermetallic constituent particles and dispersoids in aerospace aluminium alloys, Corros. Sci. 177 (2020), 108947, https://doi.org/10.1016/j.corsci.2020.108947.
[26] A.E. Hughes, A. Boag, A.M. Glenn, D. McCulloch, T.H. Muster, C. Ryan, C. Luo, X. Zhou, G.E. Thompson, Corrosion of AA2024-T3 part II: co-operative corrosion, Corros. Sci. 53 (2011) 27–39, https://doi.org/10.1016/j.corsci.2010.09.030.
[27] A.M. Glenn, T.H. Muster, C. Luo, X. Zhou, G.E. Thompson, A. Boag, A.E. Hughes, Corrosion of AA2024-T3 Part III: Propagation, Corros. Sci. 53 (2011) 40–50, https://doi.org/10.1016/j.corsci.2010.09.035.
[28] C. Luo, X. Zhou, G.E. Thompson, A.E. Hughes, Observations of intergranular corrosion in AA2024-T351: {T}he influence of grain stored energy, Corros. Sci. 61 (2012) 35–44, https://doi.org/10.1016/j.corsci.2012.04.005.
[29] R. Bonzom, R. Oltra, Intergranular corrosion propagation rate of 2024 alloy investigated via the "one-dimensional artificial pit" technique, Corros. Sci. 111 (2016) 850–855, https://doi.org/10.1016/j.corsci.2016.05.033.
[30] M.-L. de Bonfils-Lahovary, L. Laffont, C. Blanc, Characterization of intergranular corrosion defects in a 2024 T351 aluminium alloy, Corros. Sci. 119 (2017) 60–67, https://doi.org/10.1016/j.corsci.2017.02.020.
[31] R. Oltra, R. Bonzom, Real-time monitoring of intergranular corrosion damage on AA2024, CORROSION 73 (2017) 1250–1257, https://doi.org/10.5006/2496.
[32] M.-L. de Bonfils-Lahovary, C. Josse, L. Laffont, C. Blanc, Influence of hydrogen on the propagation of intergranular corrosion defects in 2024 aluminium alloy, Corros. Sci. 148 (2019) 198–205, https://doi.org/10.1016/j.corsci.2018.12.019.
[33] D. Zhu, W.J. van Ooij, Corrosion protection of AA 2024-T3 by bis-[3-(triethoxysilyl)propyl]tetrasulfide in neutral sodium chloride solution. Part 1: corrosion of AA 2024-T3, Corros. Sci. 45 (2003) 2163–2175, https://doi.org/10.1016/s0010-938x(03)00060-x.
[34] F.H. Scholes, S.A. Furman, A.E. Hughes, T.A. Markley, Corrosion in artificial defects. I: Development of corrosion, Corros. Sci. 48 (2006) 1812–1826, https://doi.org/10.1016/j.corsci.2005.05.050.
[35] F.M. Queiroz, M. Magnani, I. Costa, H.G. de Melo, Investigation of the corrosion behaviour of AA 2024-T3 in low concentrated chloride media, Corros. Sci. 50 (2008) 2646–2657, https://doi.org/10.1016/j.corsci.2008.06.041.
[36] N. Birbilis, Y.M. Zhu, S.K. Kairy, M.A. Glenn, J.-F. Nie, A.J. Morton, Y. Gonzalez-Garcia, H. Terryn, J.M.C. Mol, A.E. Hughes, A closer look at constituent induced localised corrosion in Al-Cu-Mg alloys, Corros. Sci. 113 (2016) 160–171.
[37] B. Zhang, J. Wang, B. Wu, E.E. Oguzie, K. Luo, X.L. Ma, Direct observation of atomic-scale origins of local dissolution in Al-Cu-Mg alloys, Sci. Rep. 6 (2016) 39525, https://doi.org/10.1038/srep39525.

[38] T. Hashimoto, X. Zhang, X. Zhou, P. Skeldon, S.J. Haigh, G.E. Thompson, Investigation of dealloying of S phase (Al2CuMg) in AA 2024-{T}3 aluminium alloy using high resolution 2D and 3D electron imaging, Corros. Sci. 103 (2016) 157–164, https://doi.org/10.1016/j.corsci.2015.11.013.
[39] X. Zhou, C. Luo, T. Hashimoto, A.E. Hughes, G.E. Thompson, Study of localized corrosion in AA2024 aluminium alloy using electron tomography, Corros. Sci. 58 (2012) 299–306, https://doi.org/10.1016/j.corsci.2012.02.001.
[40] P. Schmutz, G.S. Frankel, Corrosion Study of AA2024-T3 by scanning kelvin probe force microscopy and in situ atomic force microscopy scratching, J. Electrochem. Soc. 145 (1998) 2295–2306, https://doi.org/10.1149/1.1838634.
[41] A. Kreta, M. Rodošek, L.S. Perše, B. Orel, M. Gaberšček, A.Š. Vuk, In situ electrochemical AFM, ex situ IR reflection - absorption and confocal Raman studies of corrosion processes of AA 2024-T3, Corros. Sci. 104 (2016) 290–309, https://doi.org/10.1016/j.corsci.2015.12.023.
[42] N. Li, C. Dong, C. Man, J. Yao, Quantitative nuclear histomorphometric features are predictive of Oncotype DX risk categories in ductal carcinoma in situ: preliminary findings, Breast Cancer Res 21 (2019) 114, https://doi.org/10.1002/adem.201900386.
[43] C. Örnek, C. Leygraf, J. Pan, Real-time corrosion monitoring of aluminum alloy using scanning kelvin probe force microscopy, J. Electrochem. Soc. 167 (2020), 081502, https://doi.org/10.1149/1945-7111/ab8826.
[44] S.J. Garcia, X. Wu, S. van der Zwaag, A combined electrochemical impedance spectroscopy and x-ray-computed tomography study of the effect of a silyl ester on delamination and underfilm pit formation in a coated AA7050 sample, CORROSION 70 (2014) 475–482, https://doi.org/10.5006/0966.
[45] G. Acosta, L. Veleva, D. de la Fuente, Mapping the initial corrosion activity of aluminium alloy 2024-T3 in diluted substitute ocean water by localized electrochemical impedance spectroscopy, Mater. Corros. 69 (2018) 1368–1374, https://doi.org/10.1002/maco.201810109.
[46] J. Wloka, S. Virtanen, Detection of nanoscale η-MgZn2 phase dissolution from an Al-Zn-Mg-Cu alloy by electrochemical microtransients, Surf. Interface Anal. 40 (2008) 1219–1225, https://doi.org/10.1002/sia.2868.
[47] M.B. Jensen, A. Guerard, D.E. Tallman, G.P. Bierwagen, Studies of electron transfer at aluminum alloy surfaces by scanning electrochemical microscopy, J. Electrochem. Soc. 155 (2008) C324, https://doi.org/10.1149/1.2916734.
[48] Q. Zhou, Y. Wang, D.E. Tallman, M.B. Jensen, Simulation of SECM approach curves for heterogeneous metal surfaces, J. Electrochem. Soc. 159 (2012) H644–H649, https://doi.org/10.1149/2.034207jes.
[49] S. Malladi, C. Shen, Q. Xu, T. de Kruijff, E. Yücelen, F. Tichelaar, H. Zandbergen, Localised corrosion in aluminium alloy 2024-T3 using in situ TEM, Chem. Commun. (Camb.) 49 (2013) 10859–10861, https://doi.org/10.1039/c3cc46673f.
[50] A. Boag, R.J. Taylor, T.H. Muster, N. Goodman, D. McCulloch, C. Ryan, B. Rout, D. Jamieson, A.E. Hughes, Stable pit formation on AA2024-T3 in a NaCl environment, Corros. Sci. 52 (2010) 90–103, https://doi.org/10.1016/j.corsci.2009.08.043.
[51] P.J. Denissen, S.J. Garcia, Reducing subjectivity in EIS interpretation of corrosion and corrosion inhibition processes by in-situ optical analysis, Electrochim. Acta 293 (2019) 514–524, https://doi.org/10.1016/j.electacta.2018.10.018.
[52] P.J. Denissen, A.M. Homborg, S.J. Garcia, Interpreting electrochemical noise and monitoring local corrosion by means of highly resolved spatiotemporal real-time optics, J. Electrochem. Soc. 166 (2019) C3275–C3283, https://doi.org/10.1149/2.0341911jes.
[53] A.M. Homborg, E.P.M. van Westing, T. Tinga, G.M. Ferrari, X. Zhang, J.H.W. de Wit, J.M.C. Mol, Application of transient analysis using Hilbert spectra of electrochemical noise to the identification of corrosion inhibition, Electrochim. Acta 116 (2014) 355–365, https://doi.org/10.1016/j.electacta.2013.11.084.
[54] A.M. Homborg, R.A. Cottis, J.M.C. Mol, An integrated approach in the time, frequency and time-frequency domain for the identification of corrosion using electrochemical noise, Electrochim. Acta 222 (2016) 627–640, https://doi.org/10.1016/j.electacta.2016.11.018.
[55] Y. Yoon, R.G. Buchheit, Dissolution behavior of Al[sub 2]CuMg (S Phase) in chloride and chromate conversion coating solutions, J. Electrochem. Soc. 153 (2006) B151, https://doi.org/10.1149/1.2177005.
[56] J.O. Park, C.H. Paik, Y.H. Huang, R.C. Alkire, Influence of Fe-rich intermetallic inclusions on pit initiation on aluminum alloys in aerated NaCl, J. Electrochem. Soc. 146 (1999) 517–523, https://doi.org/10.1149/1.1391637.
[57] M. Liu, Y. Jin, C. Zhang, C. Leygraf, L. Wen, Density-functional theory investigation of Al pitting corrosion in electrolyte containing chloride ions, Appl. Surf. Sci. 357 (2015) 2028–2038, https://doi.org/10.1016/j.apsusc.2015.09.180.
[58] P. Campestrini, H.W. van Rooijen, E.P.M. van Westing, J.H.W. de Wit, Influence of quench delay time on the corrosion behavior of aluminium alloy 2024, Mater. Corros. 51 (2000) 616–627, https://doi.org/10.1002/1521-4176(200009)51:9<616::aid-maco616>3.0.co;2-8.
[59] P. Campestrini, E.P.M. van Westing, H.W. van Rooijen, J.H.W. de Wit, Relation between microstructural aspects of AA2024 and its corrosion behaviour investigated using AFM scanning potential technique, Corros. Sci. 42 (2000) 1853–1861, https://doi.org/10.1016/s0010-938x(00)00002-0.
[60] A. Boag, A.E. Hughes, N.C. Wilson, A. Torpy, C.M. MacRae, A.M. Glenn, T. H. Muster, How complex is the microstructure of AA2024-T3? Corros. Sci. 51 (2009) 1565–1568, https://doi.org/10.1016/j.corsci.2009.05.001.
[61] J. Wang, B. Zhang, Y.T. Zhou, X.L. Ma, Multiple twins of a decagonal approximant embedded in S-Al2CuMg phase resulting in pitting initiation of a 2024Al alloy, Acta Mater. 82 (2015) 22–31, https://doi.org/10.1016/j.actamat.2014.09.001.
[62] X. Zhang, T. Hashimoto, J. Lindsay, X. Zhou, Investigation of the de-alloying behaviour of θ-phase (Al2Cu) in AA2024-T351 aluminium alloy, Corros. Sci. 108 (2016) 85–93, https://doi.org/10.1016/j.corsci.2016.03.003.
[63] P.C. Pistorius, G.T. Burstein, Growth of corrosion pits on stainless steel in chloride solution containing dilute sulphate, Corros. Sci. 33 (1992) 1885–1897, https://doi.org/10.1016/0010-938x(92)90191-5.
[64] G.T. Burstein, P.C. Pistorius, S.P. Mattin, The nucleation and growth of corrosion pits on stainless steel, Corros. Sci. 35 (1993) 57–62, https://doi.org/10.1016/0010-938x(93)90133-2.
[65] A.R. Trueman, Determining the probability of stable pit initiation on aluminium alloys using potentiostatic electrochemical measurements, Corros. Sci. 47 (2005) 2240–2256, https://doi.org/10.1016/j.corsci.2004.09.021.
[66] J. Wang, B. Zhang, B. Wu, X.L. Ma, Size-dependent role of S phase in pitting initiation of 2024Al alloy, Corros. Sci. 105 (2016) 183–189, https://doi.org/10.1016/j.corsci.2016.01.016.
[67] Y.K. Chen-Wiegart, S. Wang, I. McNulty, D.C. Dunand, Effect of Ag-Au composition and acid concentration on dealloying front velocity and cracking during nanoporous gold formation, Acta Mater. 61 (2013) 5561–5570, https://doi.org/10.1016/j.actamat.2013.05.039.